nature materials

Letter

https://doi.org/10.1038/s41563-024-01995-w

Evidence for time-reversal symmetry-breaking kagome superconductivity

Received: 5 December 2023

Accepted: 5 August 2024

Published online: 28 August 2024

Check for updates

Hanbin Deng[1,15], Guowei Liu[1,15], Z. Guguchia[2,15], Tianyu Yang[1,15], Jinjin Liu[3,4,15], Zhiwei Wang[3,4,5] ✉, Yaofeng Xie[6], Sen Shao[7], Haiyang Ma[8], William Liège[9], Frédéric Bourdarot[10], Xiao-Yu Yan[1], Hailang Qin[8], C. Mielke III[2], R. Khasanov[2], H. Luetkens[2], Xianxin Wu[11], Guoqing Chang[7], Jianpeng Liu[12], Morten Holm Christensen[13], Andreas Kreisel[13], Brian Møller Andersen[13], Wen Huang[14], Yue Zhao[1], Philippe Bourges[9], Yugui Yao[3,4,5], Pengcheng Dai[6] & Jia-Xin Yin[1,8] ✉

Superconductivity and magnetism are often antagonistic in quantum matter, although their intertwining has long been considered in frustrated-lattice systems. Here we utilize scanning tunnelling microscopy and muon spin resonance to demonstrate time-reversal symmetry-breaking superconductivity in kagome metal $Cs(V, Ta)_3Sb_5$, where the Cooper pairing exhibits magnetism and is modulated by it. In the magnetic channel, we observe spontaneous internal magnetism in a fully gapped superconducting state. Under the perturbation of inverse magnetic fields, we detect a time-reversal asymmetrical interference of Bogoliubov quasi-particles at a circular vector. At this vector, the pairing gap spontaneously modulates, which is distinct from pair density waves occurring at a point vector and consistent with the theoretical proposal of an unusual interference effect under time-reversal symmetry breaking. The correlation between internal magnetism, Bogoliubov quasi-particles and pairing modulation provides a chain of experimental indications for time-reversal symmetry-breaking kagome superconductivity.

A kagome lattice is a lattice made of corner-sharing triangles. Initial research on kagome physics starts with its unusual quantum magnetism: the geometrical spin frustration can lead to the absence of a magnetic transition[1,2], and geometrically localized electrons can lead to flat-band ferromagnetism[3]. Early considerations[4–6] of superconductivity in materials hosting kagome lattices, intriguingly, also show an intimate relationship with magnetism, including the concepts of ferromagnetic superconductors and time-reversal symmetry-breaking (TRSB) superconductivity. Recent studies of topological kagome magnets and superconductors further push the interplay between magnetism and correlations in the kagome lattice to the frontier of quantum materials[7]. In particular, research on the CsV_3Sb_5 class of kagome superconductors has widely discussed a TRSB charge order[8–15]. However, the nature of their superconductivity ground state remains elusive. In this Letter, we report the discovery of TRSB superconductivity in the kagome metal $Cs(V, Ta)_3Sb_5$ via both magnetic and electronic probes.

The kagome superconductor[16] CsV_3Sb_5 crystallizes in the $P6/mmm$ space group, with a kagome network of vanadium cations coordinated by octahedra of Sb that is further separated by layers of Cs (Fig. 1a, inset). When 14% Ta atoms are doped into the V-kagome layer[17,18], the charge density wave order is fully suppressed and the critical temperature of superconductivity T_c is enhanced to 5 K.

A full list of affiliations appears at the end of the paper. ✉e-mail: zhiweiwang@bit.edu.cn; yinjx@sustech.edu.cn

https://doi.org/10.1038/s41563-024-01995-w

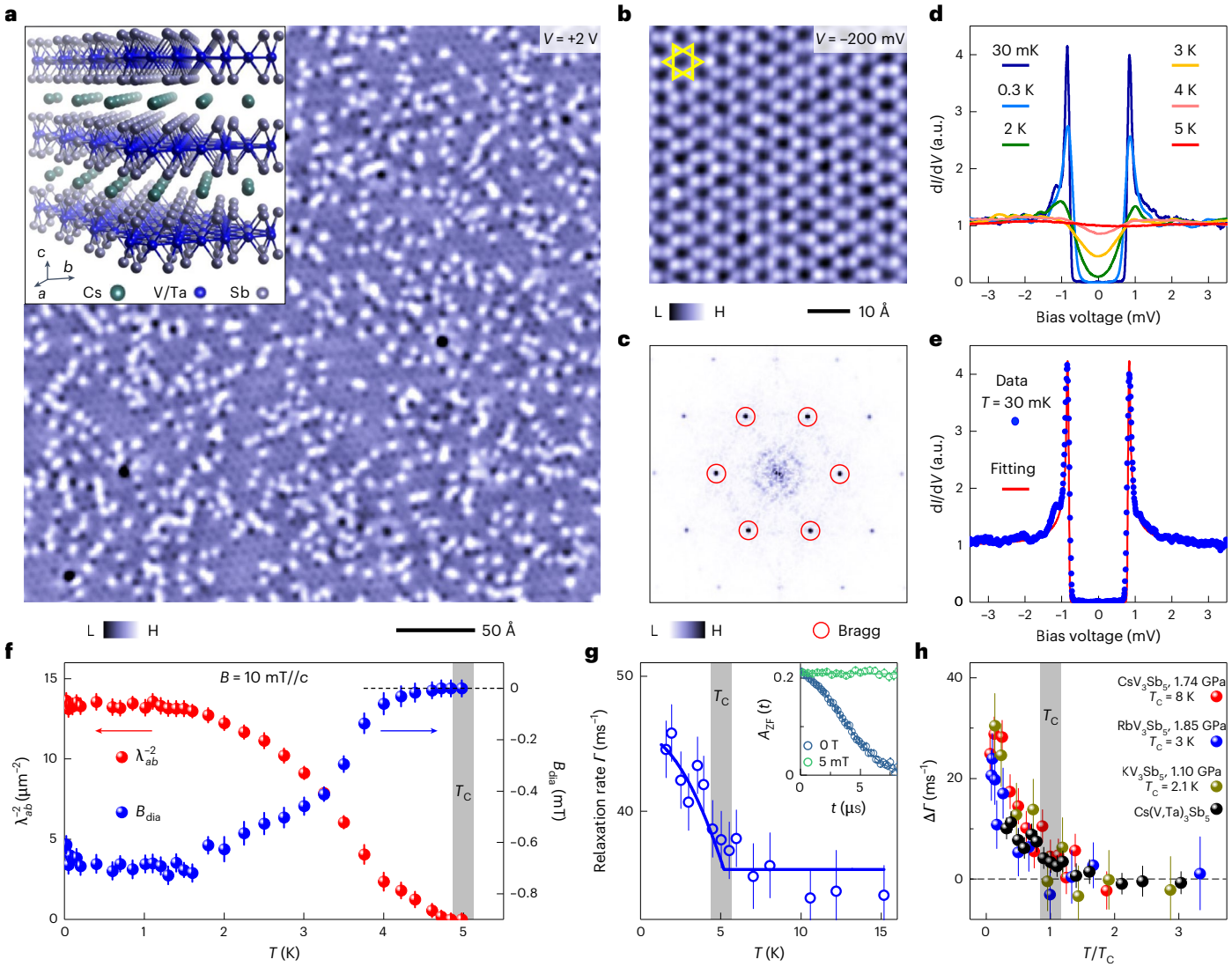

Fig. 1 | Full pairing gap and spontaneous internal magnetism. a, A topographic image of Sb surfaces taken at large bias voltage ($V = 2$ V, $I = 200$ pA, $T = 0.3$ K), showing underlying Ta dopants at bright spots. The inset shows the crystal structure of the kagome superconductor $Cs(V, Ta)_3Sb_5$. 'L' and 'H' in the colour bar define low intensity and high intensity, respectively. **b**, A topographic image showing individual Sb atoms ($V = -200$ mV, $I = 200$ pA, $T = 0.3$ K). The yellow lines illustrate the underlying kagome lattice. 'L' and 'H' in the colour bar define low intensity and high intensity, respectively. **c**, The Fourier transform of the topographic data in **b**, demonstrating the absence of 2×2 charge density wave order. The red circles mark the Bragg peaks. **d**, Differential conductance spectra taken at different temperatures ($V = 5$ mV, $I = 1$ nA). **e**, Fitting the 30 mK tunnelling data with the BCS gap function. **f**, The temperature dependence of the diamagnetic shift B_{dia} and inverse square of the in-plane penetration depth λ_{ab}^{-2} from the transverse field μSR. The magnetic field of 10 mT is applied along the *c* axis. The error bars represent the s.d. of the fit parameters. **g**, The temperature dependence of the zero-field muon spin relaxation rate, showing the spontaneous appearance of internal magnetism. The solid lines represent a heuristic guideline. The error bars represent the s.d. of the fit parameters. The inset shows the μSR time spectra $A_{ZF}(t)$ measured in zero field (dark-blue colour) and under a small external magnetic field of 50 G applied in a direction longitudinal to the muon spin polarization (green colour). The error bars are the standard error of the mean. **h**, The absolute change of the electronic relaxation rate $\Delta\Gamma = \Gamma(T) - \Gamma(T > T_C)$ for Ta-doped CsV_3Sb_5 at ambient pressure, KV_3Sb_5 at $p = 1.1$ GPa, RbV_3Sb_5 at $p = 1.85$ GPa and CsV_3Sb_5 at $p = 1.74$ GPa, plotted as a function of normalized temperature T/T_C. The error bars represent the s.d. of the fit parameters. The data for pressured kagome superconductors are extracted from refs. 14,15.

We focus our study on the Sb surface, which tightly bonds to the kagome layer and is one of the natural cleavage surfaces. Imaging at high bias voltages reveals the underlying Ta dopants, the counting of which is consistent with the nominal doping concentration (Fig. 1a). These impurities are non-magnetic and are the major scattering source for quasi-particles. Imaging at low bias voltages shows the individual Sb atoms (Fig. 1b), and the corresponding Fourier transform confirms the absence of 2×2 charge order (Fig. 1c). Probing the differential conductance deep in the superconducting state, we observe a fully opened energy gap (Fig. 1d). This gap disappears at T_C, and its lineshape at 30 mK fits with a Bardeen–Cooper–Schrieffer (BCS) gap function (Fig. 1e), both of which demonstrate it as a Cooper pairing gap. The sharp coherence peaks located at ±0.86 meV define their pairing gap size Δ_+.

The full pairing gap is further confirmed by the muon spin resonance (μSR), which is a magnetic-sensitive probe[19]. We perform transverse-field μSR experiments down to 20 mK with a field of 10 mT applied along the *c* axis (see Supplementary Information for more details). By extracting the first and second moments of the inhomogeneous field distribution from the muon spin depolarization rate, we obtain the temperature evolutions of the diamagnetism signal $B_{dia}(T)$ and the inverse square of the in-plane magnetic penetration depth

https://doi.org/10.1038/s41563-024-01995-w

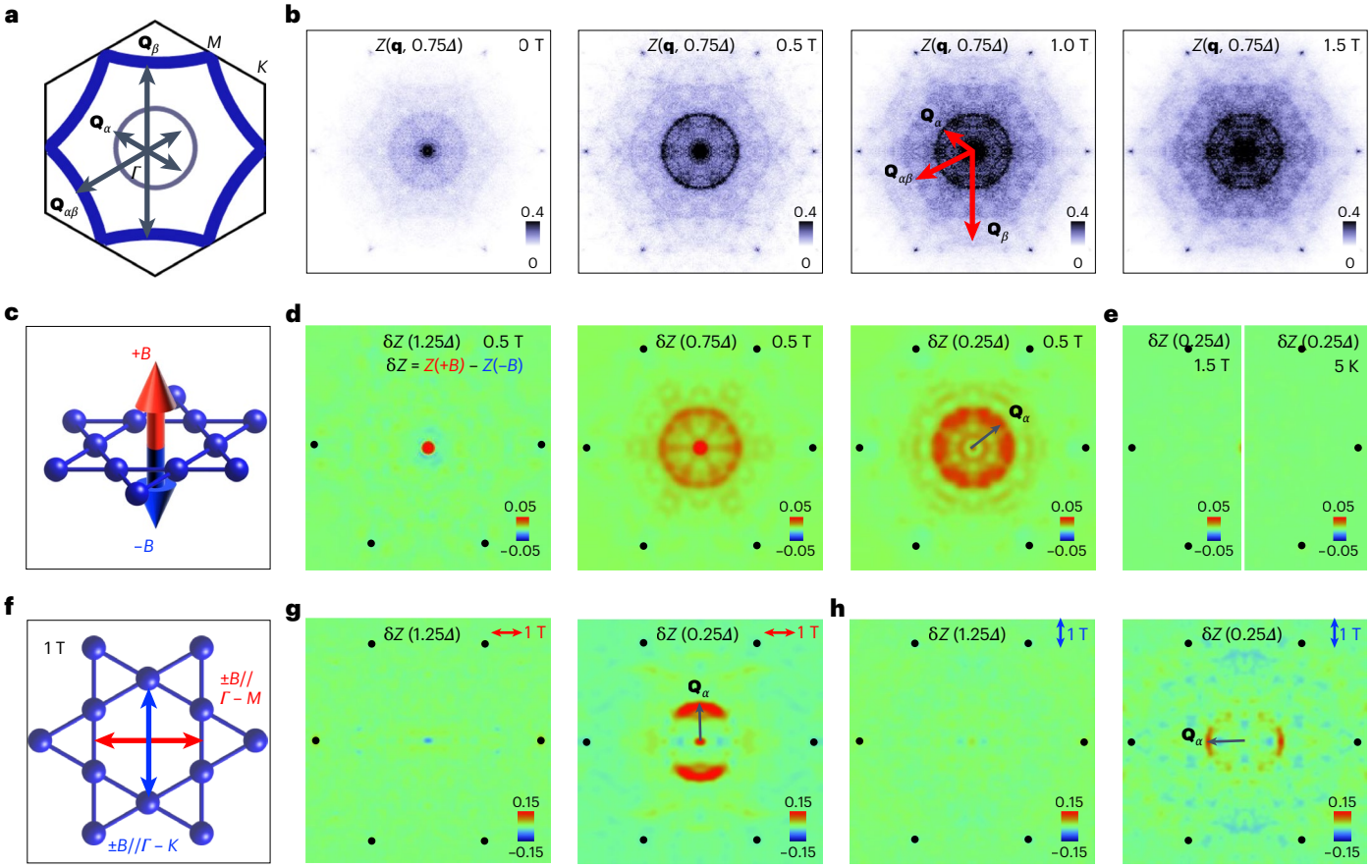

Fig. 2 | Time-reversal asymmetrical Bogoliubov quasi-particle interference. **a**, The fermiology of this kagome superconductor, which consists of the inner α band and the outer β band(s). We illustrate three main scattering vectors: $\mathbf{Q}_\alpha$, $\mathbf{Q}_\beta$ and $\mathbf{Q}_{\alpha\beta}$. **b**, The Bogoliubov quasi-particle interference $Z(\mathbf{q})$ at different magnetic fields applied along the c axis. The intensities at $\mathbf{Q}_\alpha$, $\mathbf{Q}_\beta$ and $\mathbf{Q}_{\alpha\beta}$ are all progressively increasing with increasing field strength. The data are sixfold symmetrized. **c**, An illustration of inverse magnetic fields applied perpendicular to the kagome lattice as a time-reversal perturbation of superconductivity. **d**, The time-reversal asymmetrical Bogoliubov quasi-particles interference signal δZ for $E = 1.25\Delta$ (left), $E = 0.75\Delta$ (middle) and $E = 0.25\Delta$ (right), obtained by the subtraction of Z taken with opposite fields. The signal disappears outside the superconducting gap. The data are sixfold symmetrized. The black dots mark the Bragg peak positions. **e**, The disappearance of the δZ signal at the critical magnetic field (left) and at the superconducting transition temperature (right). The data are sixfold symmetrized. The black dots mark the Bragg peak positions. **f**, An illustration of inverse magnetic fields applied along the Γ–M and Γ–K directions as a time-reversal perturbation of superconductivity. **g**,**h**, The absence of the δZ signal at the energy outside the superconducting gap (left) and the emergence of the δZ signal at the energy inside the superconducting gap (right). Reversed magnetic fields are applied along the Γ–M direction (**g**) and Γ–K direction (**h**). The data are vertically and horizontally symmetrized. All the data were taken at $V = 5$ mV, $I = 1$ nA, $T = 0.3$ K, except for the right panel of **e**, which was taken at $T = 5$ K.

$\lambda_{ab}^{-2}(T)$ (a fundamental property that is proportional to the superfluid density), respectively (Fig. 1f). Both signals emerge below T_C, indicating the bulk character of superconductivity. Notably, λ_{ab}^{-2} reaches its zero-temperature value exponentially, demonstrating full gap superconductivity.

After confirming the full gap, we employ the zero-field μSR experiments to probe whether there is TRSB in the superconducting state. Figure 1g (inset) displays the zero-field μSR spectrum, measured at $T = 1.5$ K. Since the relaxation is decoupled by a small external magnetic field (50 G) applied longitudinally to the muon spin polarization, the zero-field relaxation is due to spontaneous fields that are static on the microsecond timescale[20]. Figure 1g plots the internal field width $\Gamma(T)$, which shows a noteworthy increase upon lowering the temperature below T_C. This observation indicates the enhanced spread of internal fields sensed by the muon ensemble concurrent with the onset of superconductivity. The increase in the relaxation below T_C is estimated to be 0.012 μs^{-1}, corresponding to a characteristic field strength $\Gamma/\gamma_\mu = 0.15$ G, where γ_μ is the gyromagnetic ratio of the muon. This is comparable to what has been observed in superconductors that are believed to be TRSB, such as Sr_2RuO_4 (ref. 20). A similar enhancement of Γ below T_C has been observed[14,15] in AV_3Sb_5 (A = K, Rb, Cs) when the charge order is suppressed by pressure (Fig. 1h). However, not limited to kagome superconductors, the electronic feature of TRSB superconductivity has long been elusive.

To resolve the tiny TRSB signal from the electronic structure, we designed magneto-electronic interference experiments at 0.3 K running for 4 months. The key fermiology of this kagome superconductor, which consists of an inner α band and outer β band(s), is shown in Fig. 2a. Three dominant backscattering vectors ($\mathbf{Q}_\alpha$, $\mathbf{Q}_\beta$ and $\mathbf{Q}_{\alpha\beta}$) arising from these two sets of Fermi surfaces are seen by our experiments, as shown below. We collect the tunnelling conductance $g(\mathbf{r}, E)$ under different magnetic fields for a large field of view (~500 Å × 500 Å). We then map a ratio[21,22] $Z(\mathbf{r}, E) = g(\mathbf{r}, +E)/g(\mathbf{r}, -E)$, the process of which selects the Bogoliubov quasi-particle interference featuring a particle–hole symmetry. We collect these maps at $E = 0.75\Delta$ with increasing c-axis magnetic field up to above its critical field (1.5 T). Through the Fourier transformation of these maps, we obtain the field-dependent Bogoliubov quasi-particle interference $Z(\mathbf{q})$ in Fig. 2b. They show a progressive increment of Bogoliubov quasi-particle scatterings at three $\mathbf{Q}$ vectors with increasing field.

https://doi.org/10.1038/s41563-024-01995-w

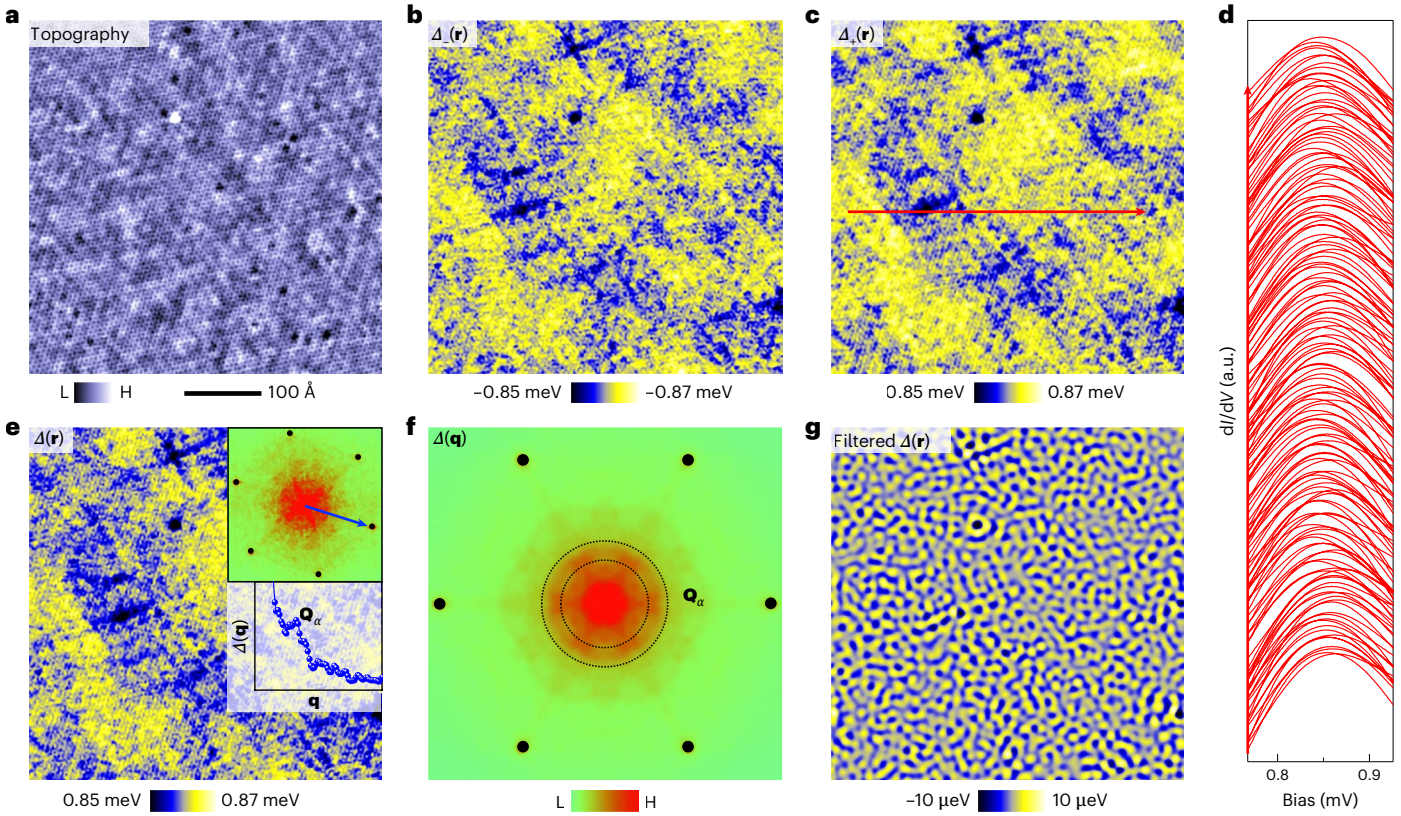

Fig. 3 | Spontaneous Cooper pairing modulation. a, A topographic image for a clean Sb surface, where the following gap map is taken. **b**, The energy map of the superconducting coherence peak at negative bias $\Delta_-(\mathbf{r})$. **c**, The energy map of the superconducting coherence peak at positive bias $\Delta_+(\mathbf{r})$. The line with an arrow denotes where the line spectrums are taken. **d**, Spectra of the positive coherence peak along the line in **c**. From the peak position of each curve, we determine Δ_+ at each location. Spectra are offset for clarity. **e**, The superconducting gap map $\Delta(\mathbf{r}) = [\Delta_+(\mathbf{r}) - \Delta_-(\mathbf{r})]/2$. The upper inset shows its Fourier transform, with an arrow along the Bragg direction, and the lower inset shows the corresponding line cut with a state at $\mathbf{Q}_\alpha$. **f**, The sixfold-symmetrized Fourier transform of the gap map. The dashed lines mark $\mathbf{Q}_\alpha$ in between. **g**, The Inverse Fourier transform of $\Delta(\mathbf{q})$ for the areas around $\mathbf{Q}_\alpha$ in the inset of **e**. All the data were taken at $V = 5$ mV, $I = 1$ nA, $T = 0.3$ K.

Based on the magnetic sensitivity of $Z(\mathbf{q})$, we further design an interference experiment with an innovative TRSB-sensitive setup as shown in Fig. 2c. We collect $Z(\mathbf{q})$ data with opposite c-axis fields $+B$ and $-B$. Then, we look at their signal difference ($\delta Z(\mathbf{q}) = Z(\mathbf{q}, +B) - Z(\mathbf{q}, -B)$), which defines the time-reversal asymmetrical interference of Bogoliubov quasi-particles. In the middle ($E = 0.75\Delta$) and right ($E = 0.25\Delta$) panels of Fig. 2d, we indeed observe a TRSB signal $\delta Z(\mathbf{q})$ at a circular vector $\mathbf{q} = \mathbf{Q}_\alpha$, under $B = \pm 0.5$ T. We note that $\delta Z/Z = 12 \pm 2\%$, which is orders of magnitude larger than the random noise of the Z signal on the level of 0.1–1%. This TRSB signal disappears at energies outside the pairing gap (Fig. 2d, left, $E = 1.25\Delta$), at the critical magnetic field (Fig. 2e, left), and at T_C (Fig. 2e, right) (see Supplementary Information for more data and discussions). We further explore its behaviour with reversed in-plane fields $B = \pm 1$ T applied along two high-symmetry directions: Γ–M and Γ–K (Fig. 2f–h). In the obtained $\delta Z(\mathbf{q})$ data taken at the energy outside the superconducting gap, we reconfirm the absence of $\delta Z(\mathbf{q})$ signal. Inside the superconducting gap, we observe that the time-reversal asymmetric signal at $\mathbf{Q}_\alpha$ again emerges. In addition, different from a nearly isotropic signal as in the c-axis field case, the $\delta Z(\mathbf{q})$ signal becomes two segmented arcs, which is due to the additional Doppler shift effect of in-plane field-induced screening supercurrent[23]. The TRSB setup, as well as the energy, magnetic field and temperature dependences of the $\delta Z(\mathbf{q})$ signal, attest to its intimate relation with the internal magnetism of superconductivity. Our experiment is also in line with the non-reciprocal transport and superconducting diode phenomena observed in kagome-superconductor-based devices[24–26]. These TRSB-related experiments suggest rich interplay between internal magnetism and Cooper pairs, and their response to the magnetic or electrical field applied along reverse directions (with a component parallel and antiparallel to the internal magnetism direction) can be different.

Although both experiments support the TRSB of the superconducting state, we also note a crucial difference between the internal field observation and time-reversal asymmetrical Bogoliubov quasi-particle interference. The former is detected under zero field while the latter is detected under reversed magnetic fields, and we try to fill this gap by designing a new challenging experiment for their possible connection. As the internal magnetism is spontaneous, the magnetism-sensitive Cooper pairing is also expected to exhibit spontaneous modifications at the aforementioned TRSB scattering channel[27–30]. For instance, a recent theory[28] has suggested that, under TRSB, the non-magnetic impurity can cause pairing gap modulations distinct to the pair density wave occurring at a point vector. The decisive way to check the pair modulation is by measuring the gap map. We find a large clean Sb surface (400 Å × 400 Å; Fig. 3a) and map the energy of superconducting coherence peaks at both negative bias voltage $\Delta_-(\mathbf{r})$ and positive bias voltage $\Delta_+(\mathbf{r})$ for the same field of view at 0.3 K (Fig. 3b–d). It is clear that the $\Delta_+(\mathbf{r})$ map strongly mimics the $\Delta_-(\mathbf{r})$ map, confirming the particle–hole symmetry of Cooper pairing at the atomic scale. Then, we obtain the gap map $\Delta(\mathbf{r}) = [\Delta_+(\mathbf{r}) - \Delta_-(\mathbf{r})]/2$ in Fig. 3e, showing detectable modulations. The Fourier transform of the gap map as $\Delta(\mathbf{q})$ is shown in Fig. 3f, which exhibits pronounced signals at the circular vector $\mathbf{q} = \mathbf{Q}_\alpha$. At this circular vector, its intensity exhibits a small anisotropy with stronger intensity along Bragg peak

directions, similar to that of the $\delta Z(\mathbf{q})$ signal. We further elucidate the real-space features of the Cooper pairing modulation by performing an inverse Fourier transform for $\Delta(\mathbf{q})$ at $\mathbf{Q}_\alpha$ in Fig. 3g. The real-space modulations contributing to the signal at $\mathbf{Q}_\alpha$ in $\Delta(\mathbf{q})$ are rather random, probably arising from the interplay between underlying randomly distributed non-magnetic dopants and the TRSB pairing state. While quasi-particle interference is often detected in several cuprates and iron-based superconductors, the gap modulations at similar vectors have been missing. Therefore, both $\delta Z(\mathbf{q})$ and $\Delta(\mathbf{q})$ signals can serve as electronic fingerprints of TRSB superconductivity.

It is striking to observe $\delta Z(\mathbf{q})$ and $\Delta(\mathbf{q})$ emerging predominately at the same vector $\mathbf{Q}_\alpha$ even though they are from independent measurements, which supports their common relation with the underlying internal magnetism. The former regards time-reversal asymmetrical modulation of the Bogoliubov states with perturbations from inversed magnetic fields, while the latter regards the spontaneous modulation of the Cooper pairing strength. Thus, spontaneous internal magnetism, Bogoliubov quasi-particle interference and Cooper pairing modulation are intertwined in our experiments. They establish an evidence chain for the TRSB superconductivity in this kagome metal at the experimental level. This finding is complementary to previous detection of TRBS charge order, advancing our knowledge of emergent orders featuring magnetic–electronic duality in the kagome lattice. In reference to our first-principles calculations, $\mathbf{Q}_\alpha$ is related to the intra-band scattering of the α band, which is mainly composed of V/Ta $d_{xz/yz}$ orbitals and Sb p_z orbitals (from the Sb atom within the kagome layer). Its association with TRSB is beyond consideration in a simplified kagome lattice[31–36] but is in line with the important role of p–d orbital hybridization in the electronic correlation discussed in kagome superconductors[37–40]. Microscopically, our results also suggest that the full gap superconductivity in this kagome metal may host a two-component TRSB superconducting order parameter $\Delta_1 + i\Delta_2$ (such as $s + is$, $p + ip$ and $d + id$, where i is the unit imaginary number). Under such an order parameter, impurities can induce surrounding supercurrents that form internal magnetization and modulate the pairing gap. An external magnetic field can couple with the vectorial magnetization and affect the distribution of supercurrents, modifying the superconducting electronic structures. This may further result in time-reversal asymmetrical interference of Bogoliubov quasi-particles. Given the research suggesting the lack of a well-accepted solid-state example for the simplest TRSB p-wave superconductivity and given that order parameters for canonical TRSB superconductor candidates including UTe_2 and Sr_2RuO_4 remain elusive, we expect substantial theoretical efforts to be required in building a model for TRSB kagome superconductivity as constrained by our experiments. Crucially, our experimental work utilizing cutting-edge techniques builds up the correspondence between internal magnetism, Bogoliubov quasi-particles and Cooper pairing, providing a powerful methodology for revealing TRSB superconductors.

Online content

Any methods, additional references, Nature Portfolio reporting summaries, source data, extended data, supplementary information, acknowledgements, peer review information; details of author contributions and competing interests; and statements of data and code availability are available at https://doi.org/10.1038/s41563-024-01995-w.

References

1. Syôzi, I. Statistics of Kagomé lattice. *Prog. Theor. Phys.* **6**, 306–308 (1951).
2. Broholm, C. et al. Quantum spin liquids. *Science* **367**, eaay0668 (2020).
3. Mielke, A. Ferromagnetic ground states for the Hubbard model on line graphs. *J. Phys. A* **24**, L73 (1991).
4. Matthias, B. T., Suhl, H. & Corenzwit, E. Ferromagnetic superconductors. *Phys. Rev. Lett.* **1**, 449–450 (1958).
5. Anderson, P. W. & Suhl, H. Spin alignment in the superconducting state. *Phys. Rev.* **116**, 898–900 (1959).
6. Ko, W.-H., Lee, P. A. & Wen, X.-G. Doped kagome system as exotic superconductor. *Phys. Rev. B* **79**, 214502 (2009).
7. Yin, J.-X., Lian, B. & Hasan, M. Z. Topological kagome magnets and superconductors. *Nature* **612**, 647–657 (2022).
8. Yu, F. H. et al. Concurrence of anomalous Hall effect and charge density wave in a superconducting topological kagome metal. *Phys. Rev. B* **104**, L041103 (2021).
9. Jiang, Y.-X. et al. Unconventional chiral charge order in kagome superconductor KV_3Sb_5. *Nat. Mater.* **20**, 1353–1357 (2021).
10. Mielke, C. et al. Time-reversal symmetry-breaking charge order in a kagome superconductor. *Nature* **602**, 245–250 (2022).
11. Guo, C. et al. Switchable chiral transport in charge-ordered kagome metal CsV_3Sb_5. *Nature* **611**, 461–466 (2022).
12. Xu, Y. et al. Three-state nematicity and magneto-optical Kerr effect in the charge density waves in kagome superconductors. *Nat. Phys.* **18**, 1470–1475 (2022).
13. Feng, X., Jiang, K., Wang, Z. & Hu, J. Chiral flux phase in the kagome superconductor AV3Sb5. *Sci. Bull.* **66**, 1384–1388 (2021).
14. Gupta, R. et al. Two types of charge order with distinct interplay with superconductivity in the kagome material CsV_3Sb_5. *Commun. Phys.* **5**, 232 (2022).
15. Guguchia, Z. et al. Tunable unconventional kagome superconductivity in charge ordered RbV_3Sb_5 and KV_3Sb_5. *Nat. Commun.* **14**, 153 (2023).
16. Ortiz, B. R. et al. CsV_3Sb_5: a Z_2 topological kagome metal with a superconducting ground state. *Phys. Rev. Lett.* **125**, 247002 (2020).
17. Zhong, Y. et al. Nodeless electron pairing in CsV_3Sb_5-derived kagome superconductors. *Nature* **617**, 488–492 (2023).
18. Luo, Y. et al. A unique van Hove singularity in kagome superconductor $CsV_{3-x}Ta_xSb_5$ with enhanced superconductivity. *Nat. Commun.* **14**, 3819 (2023).
19. Guguchia, Z., Khasanov, R. & Luetkens, H. Unconventional charge order and superconductivity in kagome-lattice systems as seen by muon-spin rotation. *npj Quantum Mater.* **8**, 41 (2023).
20. Luke, G. M. et al. Time-reversal symmetry-breaking superconductivity in Sr_2RuO_4. *Nature* **394**, 558–561 (1998).
21. Hanaguri, T., Niitaka, S., Kuroki, K. & Takagi, H. Unconventional *s*-wave superconductivity in Fe(Se,Te). *Science* **328**, 474–476 (2010).
22. Kohsaka, Y. et al. How Cooper pairs vanish approaching the Mott insulator in $Bi_2Sr_2CaCu_2O_{8+\delta}$. *Nature* **454**, 1072–1078 (2008).
23. Zhu, Z. et al. Discovery of segmented Fermi surface induced by Cooper pair momentum. *Science* **374**, 1381–1385 (2021).
24. Wu, Y. et al. Nonreciprocal charge transport in topological kagome superconductor CsV_3Sb_5. *npj Quantum Mater.* **7**, 105 (2022).
25. Wang, Y. et al. Anisotropic proximity-induced superconductivity and edge supercurrent in kagome metal, $K_{1-x}V_3Sb_5$. *Sci. Adv.* **9**, eadg7269 (2023).
26. Le, T. et al. Superconducting diode effect and interference patterns in kagome CsV_3Sb_5. *Nature* **630**, 64–69 (2024).
27. Yu, L. Bound state in superconductors with paramagnetic impurities. *Acta Phys. Sin.* **21**, 75–91 (1965).
28. Gao, Z.-Q., Lin, Y.-P. & Lee, D.-H. Pair-breaking scattering interference as a mechanism for superconducting gap modulation. Preprint at https://arxiv.org/abs/2310.06024v1 (2023).
29. Gu, Q. et al. Detection of a pair density wave state in UTe_2. *Nature* **618**, 921–927 (2023).
30. Chen, H. et al. Roton pair density wave in a strong-coupling kagome superconductor. *Nature* **599**, 222–228 (2021).

31. Yu, S.-L. & Li, J.-X. Chiral superconducting phase and chiral spin-density-wave phase in a Hubbard model on the kagome lattice. *Phys. Rev. B* **85**, 144402 (2012).
32. Kiesel, M. L. & Thomale, R. Sublattice interference in the kagome Hubbard model. *Phys. Rev. B* **86**, 121105 (2012).
33. Wang, W.-S., Li, Z.-Z., Xiang, Y.-Y. & Wang, Q.-H. Competing electronic orders on kagome lattices at van Hove filling. *Phys. Rev. B* **87**, 115135 (2013).
34. Wu, X. et al. Nature of unconventional pairing in the kagome superconductors AV_3Sb_5 (A = K, Rb, Cs). *Phys. Rev. Lett.* **127**, 177001 (2021).
35. Tazai, R., Yamakawa, Y., Onari, S. & Kontani, H. Mechanism of exotic density-wave and beyond-Migdal unconventional superconductivity in kagome metal AV_3Sb_5 (A = K, Rb, Cs). *Sci. Adv.* **8**, eabl4108 (2022).
36. Rømer, A. T., Bhattacharyya, S., Valentí, R., Christensen, M. H. & Andersen, B. M. Superconductivity from repulsive interactions on the kagome lattice. *Phys. Rev. B* **106**, 174514 (2022).
37. Jeong, M. Y. et al. Crucial role of out-of-plane Sb *p* orbitals in Van Hove singularity formation and electronic correlations in the superconducting kagome metal CsV_3Sb_5. *Phys. Rev. B* **105**, 235145 (2022).
38. Li, H. et al. Discovery of conjoined charge density waves in the kagome superconductor CsV_3Sb_5. *Nat. Commun.* **13**, 6348 (2022).
39. Han, S. et al. Orbital-hybridization-driven charge density wave transition in CsV_3Sb_5 kagome superconductor. *Adv. Mater.* **35**, 2209010 (2023).
40. Ritz, E. T., Fernandes, R. M. & Birol, T. Impact of Sb degrees of freedom on the charge density wave phase diagram of the kagome metal CsV_3Sb_5. *Phys. Rev. B* **107**, 205131 (2023).

[1]Department of Physics, Southern University of Science and Technology, Shenzhen, China. [2]Laboratory for Muon Spin Spectroscopy, Paul Scherrer Institute, Villigen PSI, Aargau, Switzerland. [3]Centre for Quantum Physics, Key Laboratory of Advanced Optoelectronic Quantum Architecture and Measurement (MOE), School of Physics, Beijing Institute of Technology, Beijing, China. [4]Beijing Key Lab of Nanophotonics and Ultrafine Optoelectronic Systems, Beijing Institute of Technology, Beijing, China. [5]International Center for Quantum Materials, Beijing Institute of Technology, Zhuhai, China. [6]Department of Physics and Astronomy and Smalley-Curl Institute, Rice University, Houston, TX, USA. [7]Division of Physics and Applied Physics, School of Physical and Mathematical Sciences, Nanyang Technological University, Singapore, Singapore. [8]Quantum Science Center of Guangdong-Hong Kong-Macao Greater Bay Area (Guangdong), Shenzhen, China. [9]Laboratoire Léon Brillouin, Université Paris-Saclay, CNRS-CEA, Gif-sur-Yvette, France. [10]MEM MDN, Université Grenoble Alpes, CEA, INAC, Grenoble, France. [11]CAS Key Laboratory of Theoretical Physics, Institute of Theoretical Physics, Chinese Academy of Sciences, Beijing, China. [12]School of Physical Science and Technology, ShanghaiTech University, Shanghai, China. [13]Niels Bohr Institute, University of Copenhagen, Copenhagen, Denmark. [14]Shenzhen Institute for Quantum Science and Engineering, Southern University of Science and Technology, Shenzhen, China. [15]These authors contributed equally: Hanbin Deng, Guowei Liu, Z. Guguchia, Tianyu Yang, Jinjin Liu.
✉e-mail: zhiweiwang@bit.edu.cn; yinjx@sustech.edu.cn

Methods

Single-crystal growth

Single crystals of $Cs(V_{0.86}Ta_{0.14})_3Sb_5$ were synthesized via the self-flux method by using $Cs_{0.4}Sb_{0.6}$ as the flux (Cs, bulk, 99.8%; V, piece, 99.999%; Ta, powder, 99.99%; Sb, shot, 99.9999%). The above materials were loaded into an alumina crucible and then heated to 1,000 °C for 200 h. After holding for 10 h, the mixture was cooled to 200 °C at 260 h at a rate of 3 K h^{-1}. When dropped down to room temperature, the furnace was turned off. To remove the flux, the obtained samples were soaked in deionized water. Finally, shiny single crystals with hexagonal features were obtained.

Scanning tunnelling microscopy

Single crystals with sizes up to 3 mm × 3 mm × 1 mm were cleaved mechanically in situ at 10 K in ultrahigh-vacuum conditions, and then immediately inserted into the microscope head, already at He^4 base temperature (4.2 K). We then further cool the microscope head to 0.3 K via a He^3-based single-shot refrigerator. The magnetic field was applied with a small ramping speed of 1 T per 20 min. After ramping the field to a desired value, the superconducting magnet is set in the persistent mode, after which we wait for ~1–2 h for the system to relax and then find the same atomic position and start to take spectroscopic measurements. Tunnelling conductance spectra were obtained with Ir/Pt tips using standard lock-in amplifier techniques with a root mean square oscillation voltage of V_m = 0.05 meV under applied bias voltage of V = 5 mV and tunnelling current I = 1 nA. We extensively scan each crystal for large and clean Sb surfaces, which can take up to 1 week. Topographic images were taken with the following tunnelling junction setup: V = ~−100 to −200 mV, I = ~0.05–0.5 nA. The conductance maps and gap map were obtained by taking a spectrum at each location (off feedback loop) with the following tunnelling junction setup: V = 5 mV, I = 1 nA and modulation voltage V_m = ~0.05–0.2 mV. The tunnelling spectrum at 30 mK is taken with a separate dilution refrigerator-based scanning tunnelling microscope with the same scanning and tunnelling setup, except for a modulation voltage of V_m = 0.02 mV. The symmetrization process of the data includes sixfold symmetrization and mirror symmetrization.

μSR

μSR is a magnetic-sensitive probe for internal magnetism of a many-body ordering state. The μSR experiments were carried out at the Swiss Muon Source (SμS) Paul Scherrer Institute, Villigen, Switzerland. Zero-field and transverse-field μSR experiments on the single-crystalline samples were performed on the high-field HAL-9500 and general purpose surface-muon instruments at the SμS at the Paul Scherrer Institute, Villigen, Switzerland. Zero field is dynamically obtained (compensation better than 30 mG) by a newly installed automatic compensation device. When performing measurements in zero field, the geomagnetic field or any stray fields are tabulated and automatically compensated by the automatic compensation device.

Data availability

All data are available in the main text or Supplementary Information.

Acknowledgements

We thank T. Neupert, Q. Wang, D. Bounoua and Y. Sidis for insightful discussions. We are also grateful to the full IRIG/D-phy/MEM/MDN group of CEA Grenoble who helped us with the experimental setup of neutron scattering. We acknowledge the support from the National Key R&D Program of China (nos. 2023YFA1407300, 2023YFF0718403, 2022YFA1403400 and 2020YFA0308800), the National Science Foundation of China (nos. 12374060, 12321004 and 12234003) and Guangdong Provincial Quantum Science Strategic Initiative (no. GDZX2201001). Z.W. also acknowledges the Beijing Natural Science Foundation (grant no. Z210006), the Beijing National Laboratory for Condensed Matter Physics (grant no. 2023BNLCMPKF007) and the Analysis and Testing Center at BIT for assistance in facility support. Work at Nanyang Technological University was supported by the National Research Foundation, Singapore, under its Fellowship Award (no. NRF-NRFF13-2021-0010), the Agency for Science, Technology and Research (A*STAR) under its Manufacturing, Trade and Connectivity (MTC) Individual Research Grant (IRG) (grant no. M23M6c0100), Singapore Ministry of Education (MOE) AcRF Tier 2 grant (grant no. MOE-T2EP50222-0014) and the Nanyang Assistant Professorship grant (grant no. NTU-SUG). P.D. is supported by the US DOE, BES under grant no. DE-SC0012311. A.K. acknowledges support by the Danish National Committee for Research Infrastructure (NUFI) through the ESS-Lighthouse Q-MAT. Z.G. acknowledges support from the Swiss National Science Foundation (SNSF) through SNSF Starting Grant (grant no. TMSGI2_211750).

Author contributions

H.D., G.L. and T.Y. conducted the scanning tunnelling microscopy experiments in consultation with J.-X.Y.; Z.G., C.M., R.K. and H.L. conducted the μSR experiments; Jinjin L. and Z.W. synthesized and characterized the transport of samples; Y.X., W.L., F.B., P.B. and P.D. conducted polarized neutron scattering experiments; S.S., H.M., G.C. and Jianpeng L. conducted first-principles calculations; X.W., M.H.C., A.K., B.M.A., W. H. and Y.Y. contributes to the theoretical understandings; X.-Y.Y. and Y.Z. contributed to the calibration of the measurement; H.D. and J.-X.Y. performed the data analysis and figure development and wrote the paper with contributions from all authors; J.-X.Y. supervised the project.

Competing interests

The authors declare no competing interests.

Additional information

Supplementary information The online version contains supplementary material available at https://doi.org/10.1038/s41563-024-01995-w.

Correspondence and requests for materials should be addressed to Zhiwei Wang or Jia-Xin Yin.

Peer review information *Nature Materials* thanks the anonymous reviewers for their contribution to the peer review of this work.